JACS Au
AN OPEN ACCESS JOURNAL OF THE AMERICAN CHEMICAL SOCIETY

pubs.acs.org/jacsau
Article

Improving the Mg Sacrificial Anode in Tetrahydrofuran for Synthetic Electrochemistry by Tailoring Electrolyte Composition

Wendy Zhang, Chaoxuan Gu, Yi Wang, Skyler D. Ware, Lingxiang Lu, Song Lin, Yue Qi, and Kimberly A. See*

Cite This: JACS Au 2023, 3, 2280−2290
Read Online
ACCESS | Metrics & More | Article Recommendations | Supporting Information

ABSTRACT: Mg^0 is commonly used as a sacrificial anode in reductive electrosynthesis. While numerous methodologies using a Mg sacrificial anode have been successfully developed, the optimization of the electrochemistry at the anode, i.e., Mg stripping, remains empirical. In practice, electrolytes and organic substrates often passivate the Mg electrode surface, which leads to high overall cell potential causing poor energy efficiency and limiting reaction scale-up. In this study, we seek to understand and manipulate the Mg metal interfaces for a more effective counter electrode in tetrahydrofuran. Our results suggest that the ionic interactions between the cation and the anion of a supporting electrolyte can influence the electrical double layer, which impacts the Mg stripping efficiency. We find halide salt additives can prevent passivation on the Mg electrode by influencing the composition of the solid electrolyte interphase. This study demonstrates that, by tailoring the electrolyte composition, we can modify the Mg stripping process and enable a streamlined optimization process for the development of new electrosynthetic methodologies.

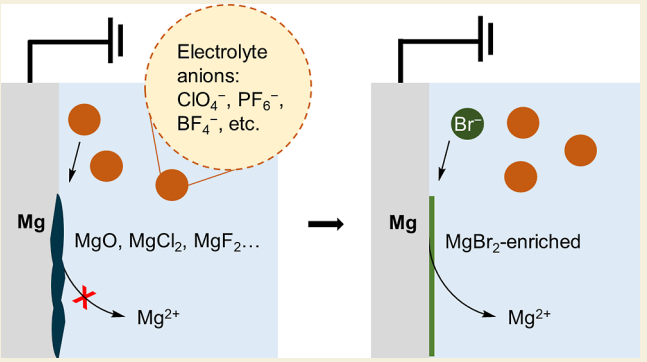

KEYWORDS: *sacrificial anode, Mg passivation, Mg stripping, tetrahydrofuran-based electrolyte, reductive electrosynthesis*

INTRODUCTION

In recent years, electrochemistry has received renewed interest in the synthetic community as a tool to prepare useful and complex organic molecules.[1−4] Electrochemistry offers unique advantages over traditional synthetic organic methods due to its ability to achieve highly selective oxidative and reductive transformations.[3] Using electrons as the reactants, electrochemistry avoids the use of harsh and often toxic traditional oxidants/reductants, giving rise to mild reaction conditions along with high atomic efficiency.[5,6] Optimizing an electrochemical reaction requires careful consideration of the reactions that occur at both the working electrode (WE) and the counter electrode (CE). The reaction occurring at the CE is called the counter reaction. For organic electrosynthesis, efficient oxidation/reduction of a sacrificial reagent is typically employed as the counter reaction.[7,8] The simplest counter reaction is metal stripping, in which a sacrificial metal electrode is simply oxidized to form soluble metal cations that dissolve into the reaction mixture.[9,10] Magnesium is commonly employed as a sacrificial anode due to its low oxidation potential (−2.37 V vs SHE), high Earth abundance, low toxicity, and apparent ease of handling on the benchtop.[10−13]

Although Mg CEs nominally involve metal stripping, side reactions can cause issues with electrochemistry. For example, supporting electrolyte anions such as ClO_4^-, PF_6^-, BF_4^-, triflate (OTf^-), and bis(trifluoromethanesulfonyl)imide ($TFSI^-$) react with Mg, generating high impedance, insoluble interphases (Figure 1).[12,14] In addition to reacting with electrolyte anions, Mg can also react with organic substrates, especially commonly used organohalides.[15] While this reactivity has proven useful for the formation of Grignard reagents, it also causes significant changes to the morphology[16,17] and composition of the Mg electrode surface. Additionally, the Mg stripping process occurs to such an extent that high concentrations of Mg^{2+} salts are formed in solution. If the solubility of the Mg^{2+} salts formed is low in the organic solvent, the salts will precipitate onto the electrode.[18] Supporting electrolyte anions are necessary for electrolyte conductivity, organohalides are often used as synthetic building blocks,[19] and the formation of Mg^{2+} is unavoidable; thus, it is challenging to maintain a stable Mg electrode interface during electrolysis. All the aforementioned reactions result in the formation of a high impedance interphase at the CE. The high-impedance interphase increases

Received: June 12, 2023
Revised: July 7, 2023
Accepted: July 11, 2023
Published: July 28, 2023

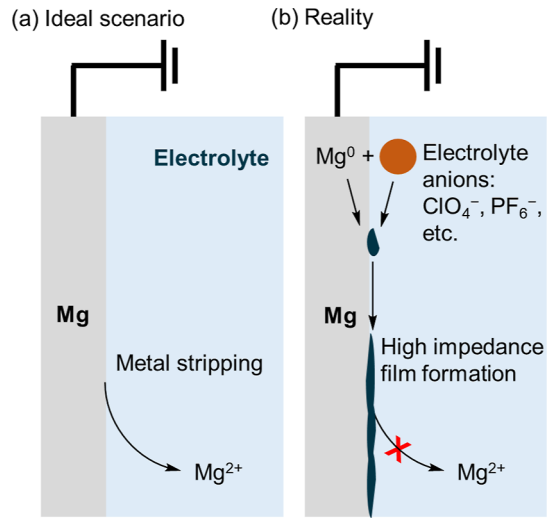

Figure 1. Mg sacrificial anodes are common CEs used in reductive organic electrosynthesis. (a) Ideally, Mg CEs undergo extensive Mg oxidation to Mg^{2+} (Mg stripping) without impediment. (b) In reality, Mg^0 reacts with the electrolyte, generating high impedance surface films that inhibit Mg stripping.

the cell voltage and lowers the efficiency of the reaction. In extreme cases, the cell voltage increases beyond the compliance limits of the potentiostat, and the reaction at the WE can no longer proceed.

To achieve effective Mg oxidation at the CE, it is therefore important to control the Mg metal interface to avoid the formation of passivating interphases. To date, there has been limited effort to address the nature of passivation or modification of reaction conditions to control the Mg interface during organic electrosynthesis. The electron transfer events at the sacrificial anode occur in a heterogeneous environment, and thus their study requires the use of research techniques not traditionally used by the organic synthetic community.[10] Traditional optimization of electrochemical reactions involves screening solvents, supporting electrolytes, and sacrificial anodes to achieve high yields of the desired product.[20] However, this approach lacks any understanding of the individual processes occurring at the electrode interfaces and thus is often met with issues of high cell voltage, which may or may not be due to the CE.

Mg sacrificial anode passivation can not only hamper the optimization of a new organic electrochemical reaction but also make reaction scale-up challenging due to the resulting high cell voltage.[18,21−28] For instance, Lin, See, and co-workers developed an electrochemically driven cross-electrophile coupling of alkyl halides.[18] Attempts to perform the electrochemical reaction on gram scale were thwarted by high anodic potential at the Mg CE due to a high impedance interphase. The interphase was composed of $MgBr_2$ and $Mg(ClO_4)_2$ as determined by various surface characterization techniques. The addition of dimethoxyethane (DME), thought to facilitate Mg^{2+} salt solvation, resulted in a decrease of Mg electrode passivation, leading to a successful scale-up of the reaction. This study demonstrates the practicality of tailoring the electrolyte by intentionally leveraging an understanding of the side reactions at the Mg CE. However, changing the solvent composition can dramatically affect the efficiency and selectivity of an organic reaction. While DME addition effectively limits the Mg anode passivation in the electrochemically driven cross-electrophile coupling reaction, it may not be a suitable solution to all reactions that require a Mg sacrificial anode. Therefore, we would like to study the Mg electrode interfaces under common organic electrosynthesis conditions to gain more insight into sacrificial anode behavior and provide promising alternative solutions to resolve the issues caused by passivation.

Here, we investigate the effect of supporting electrolytes on Mg stripping with the aim of improving Mg sacrificial anode performance in tetrahydrofuran (THF)-based electrolyte. Currently, the most commonly employed solvent for systems using Mg sacrificial anodes is dimethylformamide (DMF).[29] However, the evident solvent limitation could pose challenges when attempting to broaden the application of reductive electrosynthesis to different types of organic transformations. Additionally, due to the toxicity of DMF and the restrictions imposed by the European Commission on its use,[30] finding alternative solvents is of great interest. Recently, researchers have attempted to use THF as the optimal solvent in combination with Mg sacrificial anodes but have encountered anode passivation issues.[18,28] By studying the effects of the supporting electrolyte on Mg stripping in THF, we hope to provide insights into the fundamental factors affecting the Mg sacrificial anode performance and pave the way for the discovery of more cathodic reduction transformations that are achievable only in ethereal electrolytes. Linear sweep voltammetry (LSV) demonstrates that the supporting electrolyte choice has a significant impact on the stripping overpotential and current density. Molecular dynamics (MD) simulations reveal the influence of the ionic interaction between the cation and anion of the supporting electrolyte on the composition of the electrical double layer (EDL), which we correlate to the Mg stripping current density. X-ray photoelectron spectroscopy (XPS) of the Mg anode surface after anodic polarization reveals the formation of insulating interphases upon contact with ClO_4^-, PF_6^-, BF_4^-, and tosylate (OTs^-) anions. Inspired by Mg battery research, we use halide salts as co-supporting electrolytes to inhibit the formation of insulating interphases on the Mg electrode. XPS reveals that bromide salt addition results in a thinner interphase that is $MgBr_2$-enriched. The addition of Br^- salts improves the efficiency of Mg stripping in various electrolytes and effectively prevents organohalides from corroding the Mg electrode under electrolysis conditions.

RESULTS AND DISCUSSION

Effect of the Supporting Electrolyte Cation on Mg Stripping

To understand the effects of electrolyte composition on Mg sacrificial anode performance, we probe the Mg stripping behavior in THF with supporting electrolytes commonly employed for organic electrosynthesis using LSV. The LSV experiments are conducted in three-electrode cells with a Mg plate WE, graphite CE, and Pt|Fc/Fc^+ reference electrode (RE) (Figure 2a). All potentials referenced hereafter are vs the Pt|Fc/Fc^+ RE unless otherwise noted. First, we sweep the voltage positive from the open-circuit voltage (OCV) to 0.3 V at 5 mV s^{-1}. At this point, the electrode has been anodically polished to expose fresh Mg metal. Following the oxidation, the cell rests at OCV for 10 min, allowing the freshly exposed Mg metal to chemically react with the electrolyte. The LSV−OCV protocol is repeated 5 times and the resulting 5th LSV is

https://doi.org/10.1021/jacsau.3c00305
JACS Au 2023, 3, 2280−2290

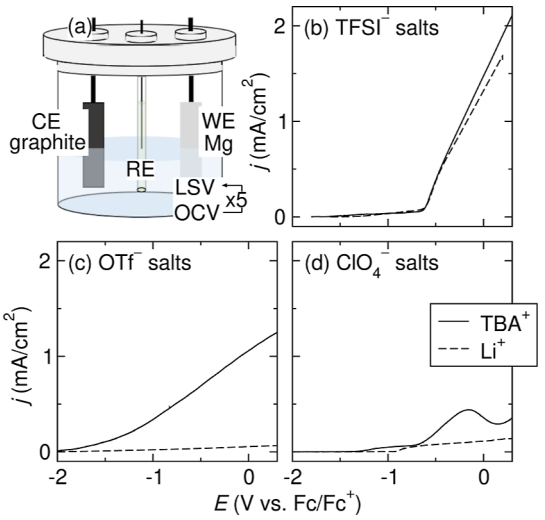

Figure 2. (a) Schematic of the three-electrode cell with a Mg WE, graphite CE, Pt|Fc/Fc$^+$ RE, and 0.1 M supporting electrolyte in 7 mL of THF. Linear sweep voltammograms of Mg stripping in Li$^+$/TBA$^+$ electrolytes with (b) TFSI$^-$, (c) OTf$^-$, and (d) ClO_4^- anions. All voltammograms are collected at a scan rate of 5 mV s^{-1}. Generally, the TBA$^+$ electrolytes yield higher anodic current densities.

shown in Figure 2. The prior LSVs are shown in the Supporting Information. All onset potentials and current densities at 0.2 V of the LSV experiments are tabulated in Table 1.

To understand how the cations of the supporting electrolyte affect Mg stripping, we compare the LSVs obtained in electrolytes with tetrabutylammonium (TBA$^+$) and Li$^+$ cations. TBA$^+$ and Li$^+$ salts with weakly coordinating anions are popular supporting electrolytes for organic electrosynthesis due to their high solubility in polar aprotic solvents and minimal interference with organic reactions.[1] Figure 2 shows the LSVs of Mg stripping in TBA$^+$/Li$^+$ electrolytes with TFSI$^-$, OTf$^-$, and ClO_4^- anions. Interestingly, the Li$^+$ electrolytes consistently yield lower current densities for Mg stripping compared to the TBA$^+$ electrolytes with the same anions. The current density additionally depends on the anion. While the current densities for Mg stripping are comparable in LiTFSI and TBATFSI electrolytes, TBA$^+$ electrolytes support much higher current densities with OTf$^-$ and ClO_4^- anions compared to their Li$^+$ counterparts. The low conductivities of LiOTf and $LiClO_4$ electrolytes (16.5 and 62.6 μS/cm, respectively) could be responsible for the poor Mg stripping behavior. However, LSVs with *iR* compensation show that the Li$^+$ electrolytes afford much lower current densities for Mg stripping (see Supporting Information), indicating that low electrolyte conductivity does not explain the observed cation effect. We next hypothesize that the observed Mg stripping behavior stems from the ionic interaction between TBA$^+$/Li$^+$ and the anions in the electrolytes. Compared to TBA$^+$, Li$^+$ presumably forms stronger ionic bonds with the anions in the electrolyte due to its greater charge density.[31] The strength of the ionic interactions can change the composition of the EDL at the Mg electrode surface, which may affect the Mg stripping process.

To experimentally probe the effects of cation identity on ionic interactions in the bulk electrolyte, we measure the Raman spectra of the solutions. Figure 3a,b shows the Raman spectra of TBATFSI and LiTFSI in THF. We measure the electrolytes at the concentration that is used for the electrochemistry, 0.1, and 0.5 M to observe greater signal to noise. In all cases, the speciation does not shift significantly between the 0.1 and the 0.5 M solutions. The TBATFSI solution has only one mode at 742 cm^{-1} (mode a). Mode a can be assigned to the symmetric bending mode, δ_s, of the CF_3 in free (i.e., uncoordinated) TFSI$^-$ with minimal interactions with the cation.[31] However, the LiTFSI solution has two modes, including mode a and a new mode at 747 cm^{-1} (mode b). Mode b is the same $\delta_s CF_3$ mode in the TFSI$^-$, but it is shifted due to coordination with the Li$^+$.[31] The TBATFSI

Table 1. Conductivity (σ), Onset Potential (E_{on}), and Current Density (j) of Mg Stripping in THF with Various Supporting Electrolytes

supporting electrolyte[a]	σ (μS/cm)[b]	E_{on} (V vs Fc/Fc$^+$)[c]	j (mA/cm^2)[d]	Figure refs.
LiTFSI	869.0	−0.65	1.69	Figure 2b
TBATFSI	846.6	−0.65	1.90	Figure 2b
LiOTf	16.5			Figure 2c
TBAOTf	327.0	−1.70	1.19	Figure 2c
$LiClO_4$	62.6	−0.90	0.13	Figure 2d
$TBAClO_4$	289.6	−0.69	0.30	Figure 5a
$TBAClO_4$ + LiBr	157.8	−2.37	1.21	Figure 5a
$TBAClO_4$ + TBABr	212.7	−2.45	1.60	Figure 5a
TBAOTs	109.0			Figure 5b
TBAOTs + LiBr	52.6	−1.46	0.26	Figure 5b
TBAOTs + TBABr	110.5	−1.42	0.60	Figure 5b
$TBAPF_6$	506.3			Figure 5c
$TBAPF_6$ + LiBr	308.4	−2.36	1.72	Figure 5c
$TBAPF_6$ + TBABr	346.3	−2.47	1.57	Figure 5c
$TBAPF_6$ + LiCl	254.2	−0.91	0.92	Figure S3
$TBAPF_6$ + LiI	272.4	−2.25	0.64	Figure S3
$TBABF_4$	288.5			Figure 5d
$TBABF_4$ + LiBr	118.0	−1.41	0.23	Figure 5d
$TBABF_4$ + TBABr	219.2	−1.57	1.08	Figure 5d

[a]The electrolyte is THF with 0.1 M supporting electrolyte of interest or 0.05 M supporting electrolyte + 0.05 M halide salt additive. [b]Conductivity is measured at 22.0 ± 1.0 °C. [c]E_{on} is defined as the potential at which dj/dE exceeds 0.3. [d]j at 0.2 V is reported.

https://doi.org/10.1021/jacsau.3c00305
JACS Au 2023, 3, 2280−2290

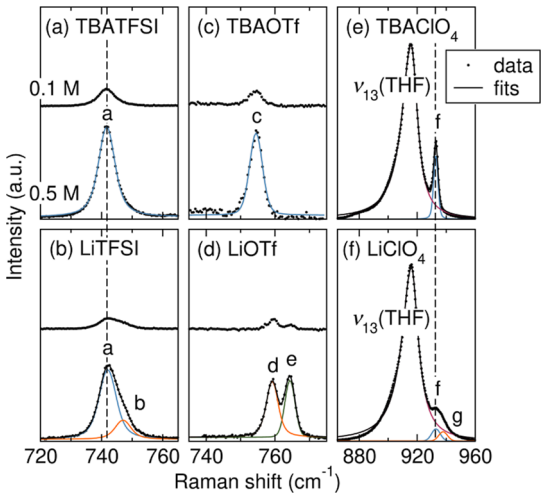

Figure 3. Raman spectra of (a) TBATFSI, (b) LiTFSI, (c) TBAOTf, (d) LiOTf, (e) $TBAClO_4$, and (f) $LiClO_4$ electrolytes at 0.1 and 0.5 M in THF. Dashed lines indicate positions of the free $TFSI^-$ and ClO_4^- anion modes and are guides for the eye.

electrolyte exhibits only the free $TFSI^-$ mode, indicating weak ionic interactions between TBA^+ and $TFSI^-$. Deconvolution of the δ_sCF_3 band of the LiTFSI electrolyte (0.5 M) shows the presence of both free $TFSI^-$ (80%) and Li^+ coordinated $TFSI^-$ (20%). The high concentration of free $TFSI^-$ in LiTFSI electrolyte indicates the ionic interaction between Li^+ and $TFSI^-$ is relatively weak. Figure 3c,d shows the Raman spectra of TBAOTf and LiOTf in THF. The TBAOTf electrolyte has one mode at 755 cm^{-1} (mode c), ascribed to the δ_sCF_3 in free OTf^-.[32] The LiOTf electrolyte exhibits two modes, both shifted from the frequency associated with free OTf^-. The modes are at 759 cm^{-1} (mode d) and 764 cm^{-1} (mode e), which are assigned to Li^+ coordinated OTf^- (58%) and multiple ion pair aggregates (42%), respectively.[32] The complete disappearance of free OTf^- in the LiOTf Raman spectrum (Figure 3d) suggests strong ionic bonding interactions between Li^+ and OTf^-. Figure 3e,f shows the Raman spectra of $TBAClO_4$ and $LiClO_4$ in THF. The strong mode at 916 cm^{-1} is the ring breathing mode of the THF solvent.[33,34] Another mode is observed at 933 cm^{-1} (mode f) that partially overlaps with the solvent mode. Mode f is assigned to the symmetric stretching mode, υ_s, of the ClO_4^-.[35] The $LiClO_4$ electrolyte shows the mode associated with free ClO_4^- (57%) and a new mode at 938 cm^{-1} (mode g). Mode g is assigned to solvent-separated ion pairs (43%), indicating moderate ionic interaction between Li^+ and ClO_4^-.[35] Therefore, we observe that Li^+ generally has greater interactions with the anions in the bulk electrolyte than TBA^+. All assignments of Raman shifts for the TBA^+/Li^+ electrolytes are tabulated in Table 2.

To understand how the ionic interactions in the bulk electrolyte affect the EDL at the anode, slab-geometry MD simulations are performed. The composition of each MD simulation box corresponds to a 0.5 M THF solution of each ionic species. The anode and cathode are modeled by inert graphene slabs. The realistic Mg surface is not Mg^0; instead, it is heterogeneous and usually covered by a complex SEI. Additionally, the impact of van der Waals forces between the SEI and electrolyte is relatively minor compared to the effect of the applied electric field. Therefore, we use graphene as a surrogate for the Mg electrode surface to focus on the

Table 2. Assignments of Raman Shifts for TBA^+/Li^+ Electrolytes with $TFSI^-$, OTf^-, and ClO_4^- Anions

peak ID	Raman shift (cm^{-1})	mode	assignment	refs
a	742	δ_sCF_3	free $TFSI^-$	31
b	747	δ_sCF_3	Li^+ coordinated $TFSI^-$	31
c	755	δ_sCF_3	free OTf^-	32
d	759	δ_sCF_3	Li^+ coordinated OTf^-	32
e	764	δ_sCF_3	Li^+OTf^- ion pair aggregates	32
f	933	$\upsilon_sClO_4^-$	free ClO_4^-	35
g	938	$\upsilon_sClO_4^-$	solvent separated $Li^+ClO_4^-$ ion pair	35

influence of the electric field on the EDL structure. Prior works have used similar approaches to represent Li and Zn electrodes with graphene in MD simulations.[36−38] As the graphene slabs are polarized, we observe changes in the electrolyte. Figure 4

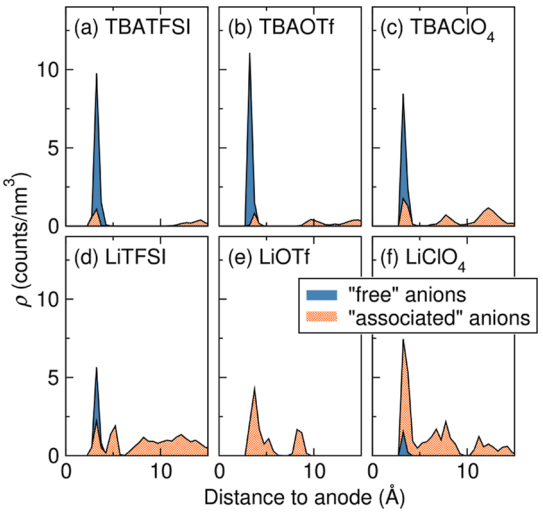

Figure 4. Number density of anions near the positively charged anode surface as calculated by MD for (a) TBATFSI, (b) TBAOTf, (c) $TBAClO_4$, (d) LiTFSI, (e) LiOTf, and (f) $LiClO_4$ supporting electrolytes in THF. An anion is defined as "free" if its distance to any cation is higher than a defined cutoff value, otherwise it is considered "associated." The cutoffs are obtained from the radial distribution functions (RDFs) in bulk simulations. Generally, TBA^+ electrolytes have a higher density of free anions at the anode compared to Li^+ electrolytes.

shows the number density distributions of anions, categorized by their association with the cations ("associated") or lack thereof ("free"), as a function of the distance to the anode surface after polarization. The identity of the cation species dictates the concentration and the solvation state of anions near the charged anode. With the applied electric field, the positively charged electrode surface repels the TBA^+ cations, leading to free anions dominating the composition of the anode EDL (Figure 4a−c). By contrast, there are fewer free anions in the Li^+ electrolytes. The majority of the ion pairs and aggregates remain intact with the applied electric field due to their strong bonding energies. As a result, significantly fewer free anions are observed at the anode EDL in the Li^+ electrolyte (Figure 4d−f).

Comparing the LSVs to the MD simulations reveals a strong correlation between effective Mg stripping and the concentration of free anions in the anode EDL. The EDLs of

https://doi.org/10.1021/jacsau.3c00305
JACS Au 2023, 3, 2280−2290

TBATFSI and LiTFSI electrolytes both contain a significant concentration of free anions due to the weak ionic interactions between TBA^+/Li^+ and $TFSI^-$. Correspondingly, the measured current densities for Mg stripping in TBATFSI and LiTFSI electrolytes are comparable (Figure 2b). The distinction in the anode EDL composition is most significant between LiOTf and TBAOTf electrolytes. While free OTf^- anions account for >90% of the ionic species in the TBAOTf electrolyte anode EDL, Li^+ and OTf^- remain as ion pairs in the LiOTf electrolyte. The predicted EDLs correspond well to the LSV data in which TBAOTf electrolyte supports effective Mg stripping while LiOTf electrolyte only gives minimal stripping current density (Figure 2c). The moderate ionic interaction between Li^+ and ClO_4^- significantly lowers the free ClO_4^- concentration in the EDL at the anode, leading to decreased Mg stripping efficiency in $LiClO_4$ electrolyte compared to in $TBAClO_4$ electrolyte (Figure 2d). Based on these observations, we hypothesize that a high concentration of free anions at the anode surface is crucial to effective Mg stripping. The free anions likely play a role in facilitating the Mg^{2+} transfer into the electrolyte by attracting and solvating the charge dense Mg^{2+}. Efforts are ongoing to further investigate the effect of free anions on Mg^{2+} via computational methods. In the broader context of organic electrosynthesis, selecting a supporting electrolyte that has weak ionic interactions between the cations and the anions is crucial for an effective Mg sacrificial anode.

Effect of Supporting Electrolyte Anion on Mg Stripping

In addition to the cation identity, the anion identity in the supporting electrolyte strongly influences the Mg stripping in THF as well. This effect is observed in Figure 2, where both the onset potentials and current densities are drastically different in TBA^+ electrolytes with $TFSI^-$, OTf^-, or ClO_4^- anions. Compared to TBATFSI and TBAOTf, $TBAClO_4$ affords the lowest current density for Mg stripping despite the predicted high anion concentration in the EDL. We hypothesize that this effect is due to the anion and its interaction with the Mg surface. To probe the effect of anion, we expand our study to other anion choices, including OTs^-, PF_6^-, and BF_4^- anions. The LSVs for Mg stripping in these three electrolytes are shown in Figure 5. While all three electrolytes employ the TBA^+ cation, the anodic current density is very low, suggesting that they do not support Mg stripping in THF (Figure 5). All onset potentials and current densities at 0.2 V of the LSV experiments are tabulated in Table 1.

We suspect that the Mg SEI composition can influence the Mg stripping behavior in THF. The Mg SEI composition is closely related to the reactivity of the Mg anode surface with the supporting electrolyte anions. Early studies of Mg batteries suggest that supporting electrolytes based on ClO_4^-, PF_6^-, or BF_4^- are not compatible with Mg electrodes.[14] Upon anodic polarization, these anions can form insulating SEIs (presumably MgO, $MgCl_2$, or MgF_2) on the Mg anode surface, inhibiting Mg ion conduction.[12,39] To investigate the effects of anions on SEI composition, we examine the Mg anodes after anodic polarization in $TBAClO_4$, TBAOTs, and $TBAPF_6$ electrolytes via XPS.

Figure 6a–c shows the Mg 2p region of the XPS spectra measured on the Mg anode surface after anodic polarization in THF with $TBAClO_4$, TBAOTs, and $TBAPF_6$ supporting electrolytes, respectively. All peak binding energies (BEs) and assignments of the Mg 2p and other related regions are tabulated in the Supporting Information. Figure 6a reveals two

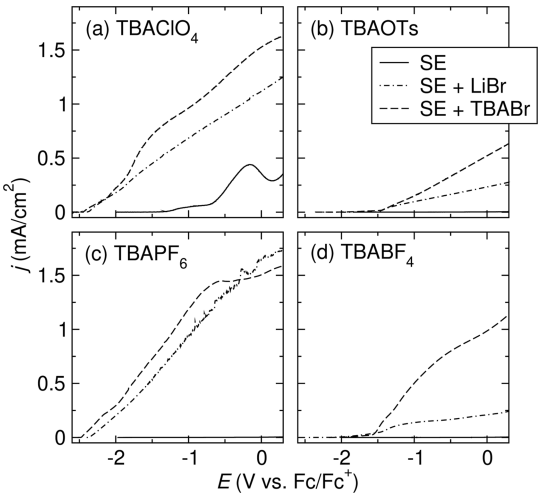

Figure 5. Linear sweep voltammograms of Mg stripping in THF with 0.1 M supporting electrolyte (SE) of interest, 0.05 M SE + 0.05 M LiBr, and 0.05 M SE + 0.05 M TBABr. The SEs are (a) $TBAClO_4$, (b) TBAOTs, (c) $TBAPF_6$, and (d) $TBABF_4$. All voltammograms are collected at a scan rate of 5 mV s^{-1}.

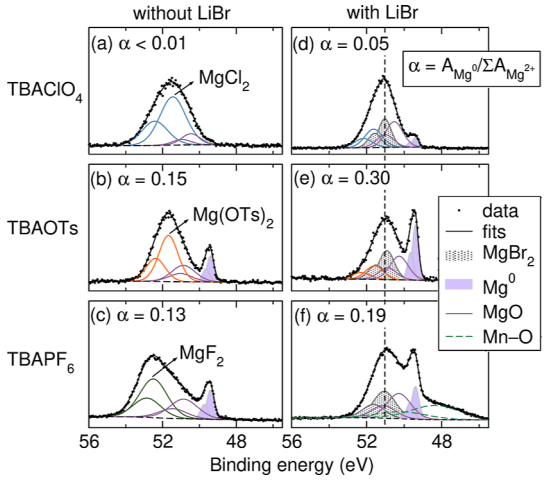

Figure 6. Mg 2p regions of the XPS spectra of Mg electrodes after the LSV experiments in THF with 0.1 M (a) $TBAClO_4$, (b) TBAOTs, and (c) $TBAPF_6$ supporting electrolytes. Mg 2p regions of the XPS spectra of Mg electrodes after the LSV experiments in THF with 0.05 M LiBr + 0.05 M (d) $TBAClO_4$, (e) TBAOTs, and (f) $TBAPF_6$ supporting electrolytes. The peak at 48.3 eV in (f) is assigned to manganese impurities in the overlapping Mn 3p region. The Mn impurity is observed due to extensive Mg stripping in $TBAPF_6$/LiBr electrolyte. α is the ratio of the area of the Mg^0 signal and the total area of Mg^{2+}-containing species signals. α provides a qualitative assessment of the thickness of the SEI, with lower α indicating thicker SEI. The dashed line indicates the position of $MgBr_2$ and is a guide for the eye.

major Mg^{2+} species in the SEI after anodic polarization in the $TBAClO_4$ electrolyte. The lower BE peak at 50.5 eV is assigned to MgO.[40] The higher BE peak at 51.4 eV is assigned to $MgCl_2$, which is likely a decomposition product derived from ClO_4^-. A trace amount of $Mg(ClO_4)_2$ is observed in the O 1s and Cl 2p regions, however, and the peak in the Mg 2p cannot be resolved from the $MgCl_2$ peak.[41] The very low-intensity peak at 49.4 eV is ascribed to Mg^0, which is difficult to see in Figure 6a. The assignment is supported by the Mg KLL Auger spectrum, where the $KL_2L_3(^1D_2)$ transition of Mg^0 is observed

https://doi.org/10.1021/jacsau.3c00305
JACS Au 2023, 3, 2280–2290

at 1185.9 eV kinetic energy (KE) (see Supporting Information).[42,43] The weak Mg^0 signal indicates a comparatively thick SEI layer, which prevents deep X-ray penetration. Figure 6b also shows two major Mg species in the SEI after anodic polarization in the TBAOTs electrolyte. Other than MgO (50.9 eV), a higher BE peak at 51.7 eV is assigned to $Mg(OTs)_2$. A small amount of reduced OTs^-, in the form of 4-methyl-sulfinate, is observed in the S 2p and O 1s spectra, but the peak cannot be resolved from $Mg(OTs)_2$ in the Mg 2p region. A relatively strong Mg^0 signal at 49.4 eV is observed, indicating a comparatively thin SEI. Figure 6c shows the presence of two Mg species in the SEI after anodic polarization in the $TBAPF_6$ electrolyte. In addition to MgO (50.9 eV), MgF_2 is observed at 52.5 eV due to the decomposition of PF_6^-.[44] The assignment is also supported by a signal at 1176.9 eV in the Mg KLL Auger spectrum (see Supporting Information), which is ascribed to MgF_2.[45] A strong Mg^0 signal (49.4 eV) is also observed, again indicating a comparatively thin SEI. MgF_2 is also the major Mg^{2+} SEI component formed in the $TBABF_4$ electrolyte (see Supporting Information). Because the SEI is similar for the $TBABF_4$ electrolyte and the $TBAPF_6$ electrolyte, we will focus only on characterizing the SEI formed in the $TBAPF_6$ electrolyte.

The species we identify in the Mg SEIs after anodic polarization are largely electronic insulators. More importantly, most of these phases are binary compounds with very low Mg^{2+} conductivity like MgO, $MgCl_2$, and MgF_2 that may prevent Mg stripping.[46−49] Interestingly, although the SEIs formed in TBAOTs and $TBAPF_6$ are thinner than that formed in $TBAClO_4$, a higher anodic current is observed when using a $TBAClO_4$ electrolyte (Figure 5). This observation highlights the importance of the composition of the SEI in affecting Mg stripping. For instance, previous studies have found that even an ultra-thin layer of MgF_2 is enough to fully passivate the Mg surface.[50]

The LSVs and XPS spectra reveal that the SEI of the Mg anode can greatly impact the anodic stripping behavior in THF. To encourage effective Mg stripping, we seek to tailor the electrolyte in hopes of manipulating the SEI composition. Mg battery research has demonstrated the beneficial effects of Cl^-, Br^-, and I^- on Mg stripping.[39] Free Cl^-, either generated through electrolyte conditioning or added in the form of metal chloride salts, can enable reversible Mg plating/stripping with low overpotential and high current density in $MgCl_2$−$AlCl_3$,[51−53] $TFSI^-$,[54,55] and PF_6^-[50] based electrolytes. Br^- additives also improve the Mg plating/stripping behavior in Mg bis(hexamethyldisilazide) based electrolyte.[56] Additionally, both Br^- and I^- additives are able to improve voltage hysteresis in Mg−S batteries by decreasing the passivation layer on the Mg anode.[39,57] We hypothesize that the halides are readily adsorbed on Mg surfaces, as this process is predicted to be exothermic.[58] Therefore, the reactive anions in the electrolyte have less access to the halide-decorated Mg surfaces, inhibiting Mg electrode passivation.[39] With this halide effect in mind, we hypothesize that the addition of halide salts as co-supporting electrolytes would affect the SEI composition of the Mg anode.

To probe the effect of halide addition, we focus on adding Br^- to the electrolyte solutions. Figure 5 shows the LSVs of the electrolytes after Br^- addition from either LiBr or TBABr. In all cases, the addition of TBABr or LiBr increases the anodic current density, suggesting that Br^- has a beneficial effect on the Mg SEI. Compared to TBABr, LiBr as the co-supporting electrolyte affords lower current densities for Mg stripping in most cases. The comparatively low current densities are likely due to Li^+ coordinating with the anions in the electrolyte, lowering the free anion concentration in the anode EDL, as discussed earlier. Cl^- and I^- additives improve Mg stripping as well (see Supporting Information). All onset potentials and current densities at 0.2 V of the LSV experiments are tabulated in Table 1.

To understand how Br^- salts affect the SEI composition, we examine the Mg anode surface after anodic polarization in TBA^+ electrolytes with LiBr additive via XPS. Figure 6d−f shows the Mg 2p regions of the XPS spectra. Three Mg species are observed in the SEI after anodic polarization in $TBAClO_4$/LiBr electrolyte (Figure 6b). The peaks at 50.5 and 51.5 eV are assigned to MgO and $MgCl_2$, respectively.[40,41] The new signal at 51.0 eV is ascribed to $MgBr_2$.[18] Comparing Figure 6a and Figure 6b, the addition of LiBr results in decreased $MgCl_2$ formation as indicated by the decrease in the proportion of $MgCl_2$ signal to the total signal from Mg^{2+} species. We also approximate the relative thickness of the SEI layers by comparing the area of Mg^{2+}-containing species to the area of the Mg^0 signal, which we give the symbol α

$$\alpha = A_{Mg^0} / \sum A_{Mg^{2+}} \quad (1)$$

Comparing Figure 6a and Figure 6b, the addition of LiBr leads to increased α (<0.01 → 0.05), indicating a comparatively thinner SEI. The addition of LiBr similarly affects the SEI formed in TBAOTs and $TBAPF_6$ electrolytes (Figure 6e,f). With LiBr, less $Mg(OTs)_2$ and MgF_2 are observed. $MgBr_2$ becomes the major Mg^{2+} species in the SEI. The new SEI is again comparatively thinner, indicated by the larger α values. The thin, $MgBr_2$-enriched SEI formed in the presence of Br^- additives likely increase the Mg^{2+} conductivity of the surface film, leading to improved Mg stripping behavior observed in Figure 5.[39] All peak BEs and assignments of the Mg 2p and other related regions are tabulated in the Supporting Information.

The results discussed above establish the correlation between the SEI composition and Mg stripping efficiency in THF. XPS spectra reveal the formation of passivating SEIs in $TBAClO_4$, TBAOTs, $TBAPF_6$, and $TBABF_4$ electrolytes. With a halide salt (Cl^-, Br^-, and I^-) co-supporting electrolyte, the modified SEIs are thinner and less passivating which facilitates effective Mg stripping. We envision that modifying the SEI composition via halide addition will have important applications in organic electrosynthesis. High cell voltage has been reported in multiple reaction developments when using a Mg sacrificial anode in $TBAClO_4$, $TBAPF_6$, and $TBABF_4$ electrolytes.[18,22−26] Our research suggests passivating SEI formation as a possible explanation for the observed high cell voltage. The use of halide co-supporting electrolytes can be a simple electrolyte tailoring strategy to improve Mg anode performance in THF in organic electrosynthesis.

Using Bromide Additives to Prevent the Reaction of Mg with Organohalides during Electrolysis

We additionally probe the utility of Br^- electrolyte additives on the performance of Mg sacrificial anodes in conditions relevant to electrosynthetic reactions. So far, we have shown that Br^- additives yield a functioning SEI and limit reaction with other components of the electrolyte, like ClO_4^-. Therefore, in our proof-of-concept experiment, we choose to evaluate conditions that demand yet another reactive species: organohalides. Among the substrates commonly used in organic electrosyn-

https://doi.org/10.1021/jacsau.3c00305
JACS Au 2023, 3, 2280−2290

thesis, organohalides are some of the most versatile yet troublesome due to their high reactivity with Mg metal.[9] While numerous electrosynthetic methodologies have been successfully developed, the high cell voltage is often observed when a Mg sacrificial anode is used for electrochemical functionalization of organohalides.[18,21,23,26] We hypothesized that during electrolysis, organohalide substrates can react directly with the Mg anode,[17] leading to the formation of a high impedance interphase. Therefore, we propose to add Br^- to the electrolyte in hopes of forming an interphase that may prevent the reaction of Mg anode with organohalides.

To probe the ability of Br^- to modulate reactivity at the Mg surface, we evaluate the effect of Br^- addition in the $TBAClO_4$ electrolyte. The $TBAClO_4$ electrolyte is a good model electrolyte because we had observed the formation of a thick crust on the surface of Mg during electrochemically driven cross-electrophile coupling of organohalides using the $TBAClO_4$-THF electrolyte.[18] The crust is absent when the reaction is performed in a divided cell, which prevents contact between the organohalide and the Mg electrode. Thus, the crust is largely due to the reaction between Mg and the organohalide. To simplify the conditions, we first probe the behavior of the Mg sacrificial anode in the same electrolyte with only the addition of a single organohalide: *tert*-butyl bromide (^{t}BuBr). A three-electrode cell with a Mg WE, graphite CE, and Ag wire pseudo-RE is used to study the voltage and impedance at the Mg electrode. The electrolyte consists of 0.5 M $TBAClO_4$ and 0.5 M ^{t}BuBr in THF. ^{t}BuBr is added as the organohalide, but also serves as a sacrificial reductant. First, galvanostatic stripping of Mg is performed for 2 h ($j \approx 1$ mA cm^{-2}), while the voltage profile at the Mg WE is recorded. Following the galvanostatic oxidation, we measure the interfacial resistance at the Mg electrode using electrochemical impedance spectroscopy (EIS). The chronopotentiometry/EIS protocol is repeated eight times to observe long-term changes in the Mg electrode performance during a typical organic electrosynthesis time frame.

Figure 7a shows the Mg stripping voltage profile in 0.5 M $TBAClO_4$/THF electrolyte in the presence of ^{t}BuBr. The potential at the Mg electrode increases drastically after 6 h and fluctuates between −1 and 4 V vs Ag wire thereafter. The initial potential increase at the Mg anode is attributed to the formation of a visibly thick passivation layer (Figure 7b), presumably consisting of $MgBr_2$ and $Mg(ClO_4)_2$ salts.[18] The salt passivation layer is structurally fragile. When the passivation layer grows to a certain limit, some of the salt crust falls off the Mg electrode surface, leading to lower interfacial resistance (see Supporting Information) and a sharp decrease of the potential. The dynamic growth and disintegration of the passivation layer are likely the cause of voltage fluctuation during galvanostatic Mg stripping.

The morphology and the surface Mg distribution of the Mg electrode surface are examined using scanning electron microscopy (SEM) and energy-dispersive X-ray spectroscopy (EDS) mapping. To reveal the surface, the $MgBr_2$ and $Mg(ClO_4)_2$ salts are first removed with acetone rinse. The SEM image and corresponding EDS map in Figure 7c show fracture formation on the Mg surface after galvanostatic Mg stripping in the presence of ^{t}BuBr. EDS mapping reveals nonuniform Mg distribution on the fractured surface, indicating uneven Mg stripping. We hypothesize that the Mg electrode is corroded upon contact with ^{t}BuBr, resulting in a rough electrode surface that has an uneven electric field distribution.[59−61] The uneven electric field distribution leads to nonuniform Mg stripping, which enhances the roughness of the electrode surface.[59,62] The fractured surface provides sites for the nucleation of Mg^{2+} salts,[63] resulting in an increase in impedance and the observed potential increase at the Mg electrode.

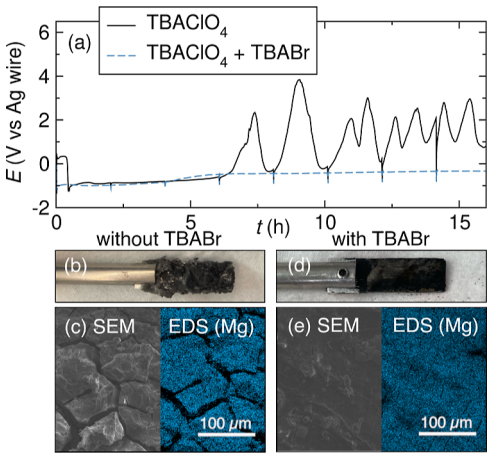

Figure 7. (a) Voltage profiles of the Mg WE during galvanostatic Mg stripping ($j \approx 1$ mA cm^{-2}) experiments in THF. The experiment is done in two electrolytes: 0.5 M $TBAClO_4$ and 0.25 M $TBAClO_4$ + 0.25 M TBABr. The electrolyte contains 0.5 M ^{t}BuBr in both cases. EIS is performed every 2 h (see Supporting Information). (b) A photograph and (c) SEM image coupled with EDS of the Mg electrode after Mg stripping in 0.5 M $TBAClO_4$ with ^{t}BuBr show a macroscopic crust and microscopic cracking. (d) A photograph and (e) SEM image coupled with EDS of the Mg electrode after Mg stripping in 0.25 M $TBAClO_4$ + 0.25 M TBABr with ^{t}BuBr show no crust and minimal cracking. The EDS maps show the surface distribution of Mg on the Mg electrodes after the galvanostatic Mg stripping experiments.

To improve the Mg stripping efficiency in the $TBAClO_4$ electrolyte and modify the SEI, TBABr is added as a co-supporting electrolyte. With TBABr, the voltage profile during galvanostatic Mg stripping remains stable between −1 and −0.5 V vs Ag wire throughout the 16 h experiment (Figure 7a). Visually, we observe minimal salt build-up on the Mg electrode at the end of the experiment (Figure 7d). The SEM image and corresponding EDS show a relatively smooth electrode surface with fractures that are much thinner. The EDS mapping reveals a more uniform Mg distribution, indicating even Mg stripping. We suggest that the Br^--rich SEI on the Mg surface functions as a protecting layer, which limits direct contact of the organohalide with the Mg anode. The success of Br^- additives shines a light on its potential application in more complex organic electrosynthesis systems that suffer from passivation build-up on the Mg sacrificial anode.

We note that other electrolyte compositions similarly prevent Mg passivation. The voltage profile of galvanostatic Mg stripping remains stable in TBATFSI and TBAOTf electrolytes (see Supporting Information), for example. The Mg anode surface maintains a smooth morphology, giving rise to minimum salt build-up on the electrode. Interestingly, these electrolytes also show large anodic current densities in the LSV experiments described above. Thus, the SEI in these electrolytes allows for efficient Mg stripping and may also prevent reactivity with organohalides.

https://doi.org/10.1021/jacsau.3c00305
JACS Au 2023, 3, 2280−2290

CONCLUSIONS

The work described here provides insights into the effect of supporting electrolytes commonly employed in organic electrosynthesis on Mg stripping in THF. The ionic interaction between the cation and the anion of the supporting electrolyte has a significant impact on the Mg stripping efficiency. When the cation is weakly coordinating (e.g., TBA^+), free anions are widely available in the electrolyte. Upon anodic polarization, the free anions migrate to the positively charged Mg anode surface, forming an EDL that has a high concentration of free anions. The free anions likely facilitate Mg^{2+} transport through the EDL, leading to higher current densities for Mg stripping. When the cation is coordinating (e.g., Li^+), the concentration of free anions is low, resulting in low Mg stripping efficiency.

However, not all TBA^+ salts result in beneficial Mg stripping. The anion of the supporting electrolyte must be considered, as well. Anions, such as ClO_4^-, OTs^-, PF_6^-, and BF_4^-, can react with the Mg surface, forming passivating SEIs that prevent effective Mg stripping. We demonstrate an effective strategy to overcome the passivating SEI. The addition of a halide (Cl^-, Br^-, and I^-) salt improves the Mg stripping significantly due to changes in the SEIs composition. For instance, the addition of Br^- yields a thinner SEI that is enriched with $MgBr_2$, both of which facilitate the Mg stripping process.

The utility of Br^- addition is extended to preventing the reaction of Mg with organohalides, a common building block in organic electrosynthesis. The extensive reaction of Mg metal with ^{t}BuBr manifests as a high impedance crust on the Mg electrode that drives up the cell voltage. The addition of Br^- prevents the formation of the crust and yields stable voltage profiles during Mg-oxidation, likely due to the SEI preventing the reaction of Mg with the organohalide. Our work demonstrates that understanding the Mg electrode interfaces is crucial to achieving good Mg sacrificial anode performance. The electrolyte tailoring strategies shown here could be used as electrolyte design principles for the optimization of new organic electrosynthetic reactions utilizing a Mg sacrificial anode.

METHODS

Electrolyte Preparation

All electrolytes were prepared in an Ar-filled glovebox. TBATFSI (≥99.0%), TBAOTf (≥99.0%), $TBAClO_4$ (≥99.0%), TBAOTs (99%), $TBAPF_6$ (≥99.0%), $TBABF_4$ (99%), TBABr (≥98.0%), LiTFSI (99.95%), LiOTf (99.995%), $LiClO_4$ (99.99%), LiBr (>99%), LiI (99.9%), and LiCl (99%) were purchased from Sigma-Aldrich. All salts were dried under vacuum at 100 °C overnight prior to use and transferred to the glovebox without exposure to air. THF (99.9%, Fischer Scientific) was dried on a solvent purification system (Pure Process Technology), transferred to the glovebox without exposure to air, and stored over dried 4 Å molecular sieves prior to use. All electrolytes were prepared by stirring the supporting electrolyte of interest in THF until the solution turned homogeneous. Electrolyte conductivity was measured in 5 mL of electrolyte in a 20 mL scintillation vial using a Metrohm 912 conductometer.

Pt|Fc/Fc$^+$ Reference Electrode Preparation

The Pt|Fc/Fc$^+$ RE was prepared following literature procedure with a 0.5 mm diameter Pt wire (Sigma-Aldrich), ferrocene (Fc, 98%, Sigma-Aldrich), ferrocenium hexafluorophosphate ($FcPF_6$, 95%, Combi-Blocks), $TBAPF_6$, and THF.[64−66] Fc and $TBAPF_6$ were recrystallized prior to use. The Pt wire, cleaned in concentrated HNO_3 and heated in a H_2 flame prior to use, was sealed within a ceramic-fritted glass tube (inner diameter 3.5 mm, Pine Research Instrumentation). The glass tube was filled with an electrolyte of 4 mM Fc, 4 mM $FcPF_6$, and 0.1 M $TBAPF_6$ in THF. The RE was assembled fresh prior to each experiment.

Electrochemical Testing

All electrochemical experiments were performed in an Ar-filled glovebox in a low volume, three-electrode cell (Pine Research Instrumentation). The Mg plate electrodes (2 mm × 8 mm × 30 mm, 99.95%, IKA) were mechanically ablated within the glovebox prior to use. LSV experiments to probe Mg stripping were performed with a Mg plate as the WE, a graphite CE (Pine Research Instrumentation), the Pt|Fc/Fc$^+$ RE, and approximately 7 mL of electrolyte. Each electrolyte was prepared with 0.1 M supporting electrolyte. Chronopotentiometry experiments were performed with a Mg WE, graphite CE, Ag wire (Pine Research Instrumentation) as a pseudo-RE, and approximately 7 mL of electrolyte. The electrolyte was prepared with 0.5 M supporting electrolyte and 0.5 M ^{t}BuBr (98%, Sigma-Aldrich) as the sacrificial oxidant. EIS experiments were performed with ±10 mV sinus amplitude from 10^6 to 1 Hz at 10 points per decade. All electrochemical experiments were conducted on a VMP3 potentiostat (Bio-Logic).

Sample Characterization

Raman spectra were collected using a HORIBA Instruments XploRA PLUS Raman spectrometer. Spectra were collected in a screw-cap cuvette to prevent exposure to air. All spectra were collected by averaging 40 acquisitions lasting 5 s each with an 1800 gr/mm grating, 50 μm slit, and 500 μm hole. The excitation wavelength was 785 nm. Peaks were fit with Voigt line shapes.[67]

SEM and EDS samples were prepared following chronopotentiometry experiments by rinsing the electrode thrice with acetone in the glovebox to dissolve adsorbed species. The electrodes were then dried in ambient glovebox conditions for 1 h. The samples were briefly exposed to air (<5 min) when loaded into the instrument. SEM data were collected on a ZEISS 1550VP field emission SEM using a 10 kV acceleration voltage and an in-lens secondary electron detector. EDS data were collected using a silicon drift EDS detector (Oxford X-MAX 80 mm^2) with a 30 kV acceleration voltage.

XPS measurements were performed on Mg anode surfaces after LSV experiments. After the LSV scans, the cells were disassembled inside an Ar-filled glovebox, and the Mg electrode was removed. Each Mg electrode was rinsed with 10 mL of THF and dried in ambient glovebox conditions for at least 48 h before analysis. The samples were briefly exposed to air (<10 s) during transfer to the XPS. XPS data were collected using a Kratos Axis Ultra system at a pressure <3 × 10^{-9} Torr. Samples were irradiated with a monochromatic Al Kα source (1486.7 eV) at 150 W. Low-resolution survey spectra were acquired between BEs of 1 and 1200 eV. Higher-resolution detailed scans, with a resolution of 0.05 eV (or 0.1 eV for Mg KLL) and a pass energy of 10 eV, were collected on individual XPS lines of interest. The XPS data were analyzed using CasaXPS analysis software, and individual peaks of interest were fit with Shirley backgrounds. Peaks were fit using mixed Gaussian−Lorentzian line shapes. Spectra were referenced to Mg^0 at 49.4 eV. The Mg^0 signal was chosen as the reference due to the complicated C 1s and O 1s signals resulting from the electrolytes.

Computational Methods

Classic MD simulations were performed by using the Forcite module in Materials Studio 2020 with COMPASS III force field (see Supporting Information for details of forcefield types).[68] The electrostatic interactions were computed using the three-dimensional Ewald summation,[69,70] and van der Waals interactions were computed using the atom-based summation with a 12.5 Å cutoff distance. Temperature control was achieved using the Nose−Hoover method,[71,72] while pressure control was achieved using the Berendsen method.[73]

To capture the electrode−electrolyte interfacial properties, slab-geometry simulation boxes were employed, where two graphene slabs served as the electrode surfaces, and the liquid electrolyte was confined between the slabs. The dimensions of the simulation box were 34.03 Å × 34.48 Å × 450.00 Å. The schematic view of the

https://doi.org/10.1021/jacsau.3c00305
JACS Au 2023, 3, 2280−2290

geometry of MD boxes is provided in Supporting Information. The distance between the slabs was adjusted to reproduce the simulated densities of bulk liquids, which are listed in Supporting Information. Periodic boundary conditions were applied in all three directions. An extra vacuum space around three times of the electrolyte length was introduced along the z direction (perpendicular to the slabs) in order to eliminate the interactions between the original box and their z-direction mirror images.[69] The constant surface charge densities of the two graphene slabs were set as ± 0.7 e/nm^2, respectively. An amorphous cell module in Materials Studio was used to build all the initial structures. We simulated six different salt species: LiTFSI, TBATFSI, LiOTf, TBAOTf, $LiClO_4$, and $TBAClO_4$. The composition of each system was 30 salt species and 800 THF molecules, corresponding to a 0.5 M THF solution.

To ensure accurate density calculations, the bulk phases in cubic boxes were relaxed using the *NPT* ensemble at 298 K and 1 bar for 1000 ps. The last 600 ps of each *NPT* trajectory was used for density calculation. Then, bulk phase systems with the calculated density were simulated under the *NVT* ensemble at 298 K for 1000 ps as the equilibrium run. Then, production runs were conducted for 3000 ps. The calculation of the cation−anion RDFs is provided in Supporting Information. The slab-geometry systems were simulated with *NVT* ensemble at 298 K for 4000 ps, with the last 3000 ps as the production run for structure analysis. The number density distributions were calculated with 0.5 Å bin size.

■ ASSOCIATED CONTENT

Supporting Information

The Supporting Information is available free of charge at https://pubs.acs.org/doi/10.1021/jacsau.3c00305.

> The complete LSV scans of Mg stripping, Nyquist plots during galvanostatic Mg stripping, additional XPS data, and computational results are given in the Supporting Information (PDF). The data that support the findings of this study are openly available in CaltechDATA at https://doi.org/10.22002/256s2-gde40.[74]

■ AUTHOR INFORMATION

Corresponding Author

Kimberly A. See − *Division of Chemistry and Chemical Engineering, California Institute of Technology, Pasadena, California 91125, United States;* orcid.org/0000-0002-0133-9693; Email: ksee@caltech.edu

Authors

Wendy Zhang − *Division of Chemistry and Chemical Engineering, California Institute of Technology, Pasadena, California 91125, United States;* orcid.org/0000-0002-6895-9598

Chaoxuan Gu − *School of Engineering, Brown University, Providence, Rhode Island 02912, United States;* orcid.org/0000-0002-2118-9805

Yi Wang − *Department of Chemistry and Chemical Biology, Cornell University, Ithaca, New York 14853, United States;* orcid.org/0000-0001-5762-5958

Skyler D. Ware − *Division of Chemistry and Chemical Engineering, California Institute of Technology, Pasadena, California 91125, United States;* orcid.org/0000-0002-3249-1946

Lingxiang Lu − *Department of Chemistry and Chemical Biology, Cornell University, Ithaca, New York 14853, United States*

Song Lin − *Department of Chemistry and Chemical Biology, Cornell University, Ithaca, New York 14853, United States;* orcid.org/0000-0002-8880-6476

Yue Qi − *School of Engineering, Brown University, Providence, Rhode Island 02912, United States;* orcid.org/0000-0001-5331-1193

Complete contact information is available at: https://pubs.acs.org/10.1021/jacsau.3c00305

Notes

The authors declare no competing financial interest.

■ ACKNOWLEDGMENTS

This work was supported by the NSF Center for Synthetic Organic Electrochemistry, CHE-2002158. XPS data were collected at the Molecular Materials Research Center in the Beckman Institute of the California Institute of Technology. K.A.S. acknowledges support from the David and Lucile Packard Foundation Fellowship for Science and Engineering. The authors thank Jake M. Evans for the assistance with collecting XPS data, and the computational resources and services provided by the Center for Computation and Visualization, Brown University.

■ REFERENCES

(1) Schotten, C.; Nicholls, T. P.; Bourne, R. A.; Kapur, N.; Nguyen, B. N.; Willans, C. E. Making Electrochemistry Easily Accessible to the Synthetic Chemist. *Green Chem.* **2020**, *22*, 3358−3375.

(2) Little, R. D.; Moeller, K. D. Introduction: Electrochemistry: Technology, Synthesis, Energy, and Materials. *Chem. Rev.* **2018**, *118*, 4483−4484.

(3) Yan, M.; Kawamata, Y.; Baran, P. S. Synthetic Organic Electrochemical Methods Since 2000: On the Verge of a Renaissance. *Chem. Rev.* **2017**, *117*, 13230−13319.

(4) Minteer, S. D.; Baran, P. Electrifying Synthesis: Recent Advances in the Methods, Materials, and Techniques for Organic Electrosynthesis. *Acc. Chem. Res.* **2020**, *53*, 545−546.

(5) Frontana-Uribe, B. A.; Little, R. D.; Ibanez, J. G.; Palma, A.; Vasquez-Medrano, R. Organic Electrosynthesis: A Promising Green Methodology in Organic Chemistry. *Green Chem.* **2010**, *12*, 2099.

(6) Yuan, Y.; Lei, A. Is Electrosynthesis Always Green and Advantageous Compared to Traditional Methods? *Nat. Commun.* **2020**, *11*, 802.

(7) Liu, J.; Lu, L.; Wood, D.; Lin, S. New Redox Strategies in Organic Synthesis by Means of Electrochemistry and Photochemistry. *ACS Cent. Sci.* **2020**, *6*, 1317−1340.

(8) Kingston, C.; Palkowitz, M. D.; Takahira, Y.; Vantourout, J. C.; Peters, B. K.; Kawamata, Y.; Baran, P. S. A Survival Guide for the "Electro-curious". *Acc. Chem. Res.* **2020**, *53*, 72−83.

(9) Chaussard, J.; Folest, J.-C.; Nedelec, J.-Y.; Perichon, J.; Sibille, S.; Troupel, M. Use of Sacrificial Anodes in Electrochemical Functionalization of Organic Halides. *Synthesis* **1990**, *1990*, 369−381.

(10) Heard, D. M.; Lennox, A. J. J. Electrode Materials in Modern Organic Electrochemistry. *Angew. Chem., Int. Ed.* **2020**, *59*, 18866−18884.

(11) Saboureau, C.; Troupel, M.; Perichon, J. Organic Electrosynthesis with a Sacrificial Anode. Chemical Reductive Degradation of the Solvent N,N-dimethyl Formamide. *J. Appl. Electrochem.* **1990**, *20*, 97−101.

(12) Gregory, T. D.; Hoffman, R. J.; Winterton, R. C. Nonaqueous Electrochemistry of Magnesium: Applications to Energy Storage. *J. Electrochem. Soc.* **1990**, *137*, 775−780.

(13) Novák, P.; Desilvestro, J. Electrochemical Insertion of Magnesium in Metal Oxides and Sulfides from Aprotic Electrolytes. *J. Electrochem. Soc.* **1993**, *140*, 140−144.

(14) Zhang, Z.; Cui, Z.; Qiao, L.; Guan, J.; Xu, H.; Wang, X.; Hu, P.; Du, H.; Li, S.; Zhou, X.; Dong, S.; Liu, Z.; Cui, G.; Chen, L. Novel Design Concepts of Efficient Mg-Ion Electrolytes toward High-Performance Magnesium-Selenium and Magnesium-Sulfur Batteries. *Adv. Energy Mater.* **2017**, *7*, 1602055.
(15) Seyferth, D. The Grignard Reagents. *Organometallics* **2009**, *28*, 1598−1605.
(16) Koon, S. E.; Oyler, C. E.; Hill, J. H. M.; Bowyer, W. J. Visualization of the Areal Distribution of the Reactivity of Magnesium Surfaces in the Formation of Grignard Reagents. *J. Org. Chem.* **1993**, *58*, 3225−3226.
(17) Teerlinck, C. E.; Bowyer, W. J. Reactivity of Magnesium Surfaces during the Formation of Grignard Reagents. *J. Org. Chem.* **1996**, *61*, 1059−1064.
(18) Zhang, W.; Lu, L.; Zhang, W.; Wang, Y.; Ware, S. D.; Mondragon, J.; Rein, J.; Strotman, N.; Lehnherr, D.; See, K. A.; Lin, S. Electrochemically Driven Cross-Electrophile Coupling of Alkyl Halides. *Nature* **2022**, *604*, 292−297.
(19) Malapit, C. A.; Prater, M. B.; Cabrera-Pardo, J. R.; Li, M.; Pham, T. D.; McFadden, T. P.; Blank, S.; Minteer, S. D. Advances on the Merger of Electrochemistry and Transition Metal Catalysis for Organic Synthesis. *Chem. Rev.* **2022**, *122*, 3180−3218.
(20) Dörr, M.; Hielscher, M. M.; Proppe, J.; Waldvogel, S. R. Electrosynthetic Screening and Modern Optimization Strategies for Electrosynthesis of Highly Value-added Products. *ChemElectroChem* **2021**, *8*, 2620.
(21) DeLano, T. J.; Reisman, S. E. Enantioselective Electroreductive Coupling of Alkenyl and Benzyl Halides via Nickel Catalysis. *ACS Catal.* **2019**, *9*, 6751−6754.
(22) Gnaim, S.; Bauer, A.; Zhang, H. J.; Chen, L.; Gannett, C.; Malapit, C. A.; Hill, D. E.; Vogt, D.; Tang, T.; Daley, R. A.; et al. Cobalt-Electrocatalytic HAT for Functionalization of Unsaturated C−C Bonds. *Nature* **2022**, *605*, 687−695.
(23) Mitsudo, K.; Nakagawa, Y.; Mizukawa, J.-i.; Tanaka, H.; Akaba, R.; Okada, T.; Suga, S. Electro-Reductive Cyclization of Aryl Halides Promoted by Fluorene Derivatives. *Electrochim. Acta* **2012**, *82*, 444−449.
(24) Franco, D.; Riahi, A.; Hénin, F.; Muzart, J.; Duñach, E. Electrochemical Reduction of a Racemic Allyl β-Keto Ester Catalyzed by Nickel Complexes: Asymmetric Induction. *Eur. J. Org. Chem.* **2002**, *2002*, 2257.
(25) Köster, F.; Dinjus, E.; Duñach, E. Electrochemical Selective Incorporation of CO2 into Terminal Alkynes and Diynes. *Eur. J. Org. Chem.* **2001**, *2001*, 3575.
(26) Harwood, S. J.; Palkowitz, M. D.; Gannett, C. N.; Perez, P.; Yao, Z.; Sun, L.; Abruña, H. D.; Anderson, S. L.; Baran, P. S. Modular Terpene Synthesis Enabled by Mild Electrochemical Couplings. *Science* **2022**, *375*, 745−752.
(27) Peters, B. K.; Rodriguez, K. X.; Reisberg, S. H.; Beil, S. B.; Hickey, D. P.; Kawamata, Y.; Collins, M.; Starr, J.; Chen, L.; Udyavara, S.; et al. Scalable and Safe Synthetic Organic Electroreduction Inspired by Li-ion Battery Chemistry. *Science* **2019**, *363*, 838−845.
(28) Huang, C.; Ma, W.; Zheng, X.; Xu, M.; Qi, X.; Lu, Q. Epoxide Electroreduction. *J. Am. Chem. Soc.* **2022**, *144*, 1389−1395.
(29) Li, Y.; Wen, L.; Guo, W. A Guide to Organic Electroreduction Using Sacrificial Anodes. *Chem. Soc. Rev.* **2023**, *52*, 1168−1188.
(30) *Commission Regulation (EU) 2021/2030 of 19 November 2021 Amending Annex XVII to Regulation (EC) No 1907/2006 of the European Parliament and of the Council Concerning the Restriction, Evaluation, Authorisation and Restriction of Chemicals (REACH) as Regards N,N-dimethylformamide*, 2021.
(31) Hardwick, L. J.; Holzapfel, M.; Wokaun, A.; Novák, P. Raman Study of Lithium Coordination in EMI-TFSI Additive Systems as Lithium-Ion Battery Ionic Liquid Electrolytes. *J. Raman Spectrosc.* **2007**, *38*, 110−112.
(32) Alía, J. M.; Edwards, H. G. Ion Solvation and Ion Association in Lithium Trifluoromethanesulfonate Solutions in Three Aprotic Solvents. An FT-Raman Spectroscopic Study. *Vib. Spectrosc.* **2000**, *24*, 185−200.
(33) Cadioli, B.; Gallinella, E.; Coulombeau, C.; Jobic, H.; Berthier, G. Geometric Structure and Vibrational Spectrum of Tetrahydrofuran. *J. Phys. Chem.* **1993**, *97*, 7844−7856.
(34) Shurvell, H.; Southby, M. Infrared and Raman Spectra of Tetrahydrofuran Hydroperoxide. *Vib. Spectrosc.* **1997**, *15*, 137−146.
(35) Kim, Y.-S.; Jeong, S.-K. Raman Spectroscopy for Understanding of Lithium Intercalation into Graphite in Propylene Carbonated-Based Solutions. *J. Spectrosc.* **2015**, *2015*, 1−5.
(36) Wu, Q.; McDowell, M. T.; Qi, Y. Effect of the Electric Double Layer (EDL) in Multicomponent Electrolyte Reduction and Solid Electrolyte Interphase (SEI) Formation in Lithium Batteries. *J. Am. Chem. Soc.* **2023**, *145*, 2473−2484.
(37) Rakov, D.; Hasanpoor, M.; Baskin, A.; Lawson, J. W.; Chen, F.; Cherepanov, P. V.; Simonov, A. N.; Howlett, P. C.; Forsyth, M. Stable and Efficient Lithium Metal Anode Cycling through Understanding the Effects of Electrolyte Composition and Electrode Preconditioning. *Chem. Mater.* **2022**, *34*, 165−177.
(38) Liu, S.; Mao, J.; Pang, W. K.; Vongsvivut, J.; Zeng, X.; Thomsen, L.; Wang, Y.; Liu, J.; Li, D.; Guo, Z. Tuning the Electrolyte Solvation Structure to Suppress Cathode Dissolution, Water Reactivity, and Zn Dendrite Growth in Zinc-Ion Batteries. *Adv. Funct. Mater.* **2021**, *31*, 2104281.
(39) Li, R.; Li, Y.; Zhang, R.; He, M.; Ma, Y.; Huo, H.; Zuo, P.; Yin, G. Voltage Hysteresis of Magnesium Anode: Taking Magnesium-Sulfur Battery as an Example. *Electrochim. Acta* **2021**, *369*, 137685.
(40) Inoue, Y.; Yasumori, I. Catalysis by Alkaline Earth Metal Oxides. III. X-Ray Photoelectron Spectroscopic Study of Catalytically Active MgO, CaO, and BaO Surfaces. *Bull. Chem. Soc. Jpn.* **1981**, *54*, 1505−1510.
(41) Fischer, P.; Reinsberg, P.; Schwarz, R. M.; Marinaro, M.; Wachtler, M.; Diemant, T.; Behm, R. J.; Baltruschat, H.; Jörissen, L. Electrochemical Formation and Characterization of Surface Blocking Layers on Gold and Platinum by Oxygen Reduction in $Mg(ClO_4)_2$ in DMSO. *J. Electrochem. Soc.* **2018**, *165*, A2037−A2046.
(42) Ley, L.; McFeely, F. R.; Kowalczyk, S. P.; Jenkin, J. G.; Shirley, D. A. Many-Body Effects in x-Ray Photoemission from Magnesium. *Phys. Rev. B: Solid State* **1975**, *11*, 600−612.
(43) Steiner, P.; Reiter, F. J.; Höchst, H.; Hüfner, S. The KLL Auger Spectra of Na and Mg Metal and Their Plasmon Structure. *Phys. Status Solidi B* **1978**, *90*, 45−51.
(44) Deifel, N. P.; Holman, K. T.; Cahill, C. L. PF6- Hydrolysis as a Route to Unique Uranium Phosphate Materials. *Chem. Commun.* **2008**, 6037.
(45) Seyama, H.; Soma, M. X-Ray Photoelectron Spectroscopic Study of Montmorillonite Containing Exchangeable Divalent Cations. *J. Chem. Soc., Faraday Trans. 1* **1984**, *80*, 237.
(46) Li, B.; Masse, R.; Liu, C.; Hu, Y.; Li, W.; Zhang, G.; Cao, G. Kinetic Surface Control for Improved Magnesium-Electrolyte Interfaces for Magnesium Ion Batteries. *Energy Storage Mater.* **2019**, *22*, 96−104.
(47) Yoo, H. D.; Shterenberg, I.; Gofer, Y.; Gershinsky, G.; Pour, N.; Aurbach, D. Mg Rechargeable Batteries: An on-Going Challenge. *Energy Environ. Sci.* **2013**, *6*, 2265.
(48) Meitav, A.; Peled, E. Solid Electrolyte Interphase (SEI) Electrode: II . The Formation and Properties of the SEI on Magnesium in Solutions. *J. Electrochem. Soc.* **1981**, *128*, 825−831.
(49) Miles, M. H.; Park, K. H.; Stilwell, D. E. Discharge and AC Impedance Studies of Lithium, Calcium, and Magnesium Anodes in Bromine Trifluoride. *J. Electrochem. Soc.* **1990**, *137*, 3393−3400.
(50) Shterenberg, I.; Salama, M.; Gofer, Y.; Aurbach, D. Hexafluorophosphate-Based Solutions for Mg Batteries and the Importance of Chlorides. *Langmuir* **2017**, *33*, 9472−9478.
(51) See, K. A.; Chapman, K. W.; Zhu, L.; Wiaderek, K. M.; Borkiewicz, O. J.; Barile, C. J.; Chupas, P. J.; Gewirth, A. A. The Interplay of Al and Mg Speciation in Advanced Mg Battery Electrolyte Solutions. *J. Am. Chem. Soc.* **2016**, *138*, 328−337.

https://doi.org/10.1021/jacsau.3c00305
JACS Au 2023, 3, 2280−2290

(52) Kim, S. S.; Bevilacqua, S. C.; See, K. A. Conditioning-Free Mg Electrolyte by the Minor Addition of $Mg(HMDS)_2$. *ACS Appl. Mater. Interfaces* **2020**, *12*, 5226−5233.
(53) Kim, S. S.; See, K. A. Activating Magnesium Electrolytes through Chemical Generation of Free Chloride and Removal of Trace Water. *ACS Appl. Mater. Interfaces* **2021**, *13*, 671−680.
(54) Shterenberg, I.; Salama, M.; Yoo, H. D.; Gofer, Y.; Park, J.-B.; Sun, Y.-K.; Aurbach, D. Evaluation of $(CF_3\ SO_2)_2\ N^-$ (TFSI) Based Electrolyte Solutions for Mg Batteries. *J. Electrochem. Soc.* **2015**, *162*, A7118−A7128.
(55) Sa, N.; Pan, B.; Saha-Shah, A.; Hubaud, A. A.; Vaughey, J. T.; Baker, L. A.; Liao, C.; Burrell, A. K. Role of Chloride for a Simple, Non-Grignard Mg Electrolyte in Ether-Based Solvents. *ACS Appl. Mater. Interfaces* **2016**, *8*, 16002−16008.
(56) Chinnadurai, D.; Lieu, W. Y.; Kumar, S.; Yang, G.; Li, Y.; Seh, Z. W. A Passivation-Free Solid Electrolyte Interface Regulated by Magnesium Bromide Additive for Highly Reversible Magnesium Batteries. *Nano Lett.* **2023**, *23*, 1564−1572.
(57) Li, X.; Gao, T.; Han, F.; Ma, Z.; Fan, X.; Hou, S.; Eidson, N.; Li, W.; Wang, C. Reducing Mg Anode Overpotential via Ion Conductive Surface Layer Formation by Iodine Additive. *Adv. Energy Mater.* **2018**, *8*, 1802041.
(58) Canepa, P.; Gautam, G. S.; Malik, R.; Jayaraman, S.; Rong, Z.; Zavadil, K. R.; Persson, K.; Ceder, G. Understanding the Initial Stages of Reversible Mg Deposition and Stripping in Inorganic Nonaqueous Electrolytes. *Chem. Mater.* **2015**, *27*, 3317−3325.
(59) Hu, Z.; Li, J.; Zhang, X.; Zhu, Y. Strategies to Improve the Performance of Li Metal Anode for Rechargeable Batteries. *Front. Chem.* **2020**, *8*, 409.
(60) Rašljić, M.; Obradov, M.; Lazić, Ž.; Vasiljević Radović, D.; Čupić, Ž.; Stanisavljev, D. Metal Layers with Subwavelength Texturing for Broadband Enhancement of Photocatalytic Processes in Microreactors. *Opt. Quantum Electron.* **2018**, *50*, 237.
(61) Tyagi, P.; Goulet, T.; Riso, C.; Klein, K.; Garcia-Moreno, F. Electropolishing of Additively Manufactured High Carbon Grade 316 Stainless Steel, **2018**. engrXiv:10.31224/osf.io/5dn49. [Preprint] August 05 [accessed 2023 July 7].
(62) Shen, X.; Zhang, R.; Chen, X.; Cheng, X.-B.; Li, X.; Zhang, Q. The Failure of Solid Electrolyte Interphase on Li Metal Anode: Structural Uniformity or Mechanical Strength? *Adv. Energy Mater.* **2020**, *10*, 1903645.
(63) Zeng, Q.; Xu, S. Thermodynamics and Characteristics of Heterogeneous Nucleation on Fractal Surfaces. *J. Phys. Chem. C* **2015**, *119*, 27426−27433.
(64) Paddon, C. A.; Compton, R. G. A Reference Electrode for Electrochemical and Cryoelectrochemical Use in Tetrahydrofuran Solvent. *Electroanalysis* **2005**, *17*, 1919−1923.
(65) Paddon, C. A.; Compton, R. G. Underpotential Deposition of Lithium on Platinum Single Crystal Electrodes in Tetrahydrofuran. *J. Phys. Chem. C* **2007**, *111*, 9016−9018.
(66) Donohoe, T. J.; Kershaw, N. M.; Baron, R.; Compton, R. G. The Effect of Ortho-Substitution on the Efficacy of Biphenyls in Mediating Electron Transfer from Lithium. *Tetrahedron* **2009**, *65*, 5377−5384.
(67) Bradley, M. *Curve Fitting in Raman and IR Spectroscopy*; Thermo Fisher Scientific, 2007.
(68) BIOVIA, Dassault Systèmes. *Materials Studio, 2020*; Dassault Systèmes: San Diego, 2020.
(69) Yeh, I.-C.; Berkowitz, M. L. Ewald Summation for Systems with Slab Geometry. *J. Chem. Phys.* **1999**, *111*, 3155−3162.
(70) Ewald, P. P. Die Berechnung optischer und elektrostatischer Gitterpotentiale. *Ann. Phys.* **1921**, *369*, 253−287.
(71) Hoover, W. G. Canonical Dynamics: Equilibrium Phase-Space Distributions. *Phys. Rev. A: At., Mol., Opt. Phys.* **1985**, *31*, 1695−1697.
(72) Nosé, S. Constant Temperature Molecular Dynamics Methods. *Prog. Theor. Phys. Suppl.* **1991**, *103*, 1−46.
(73) Berendsen, H. J. C.; Postma, J. P. M.; Van Gunsteren, W. F.; DiNola, A.; Haak, J. R. Molecular Dynamics with Coupling to an External Bath. *J. Chem. Phys.* **1984**, *81*, 3684−3690.
(74) Zhang, W.; Gu, C.; Wang, Y.; Ware, S. D.; Lu, L.; Lin, S.; Qi, Y.; See, K. Data for improving the Mg Sacrificial Anode in Tetrahydrofuran for Synthetic Electrochemistry by Tailoring Electrolyte Composition.*CaltechDATA*, DOI: 10.22002/256s2-gde40.

https://doi.org/10.1021/jacsau.3c00305
JACS Au 2023, 3, 2280−2290